Afro-Asian Journal of Scientific Research (AAJSR)
المجلة الأفروآسيوية للبحث العلمي
E-ISSN: 2959-6505
Volume 4, Issue 2, 2026
Page No: 136-152
Website: https://aajsr.com/index.php/aajsr/index
SJIFactor 2024: 5.028 ISI 2025: 0.915 معامل التأثير العربي (AIF) 2025: 0.76

An Efficient Control Strategy for Battery – Supercapacitor Hybrid Energy Storage in a PV-Based DC Microgrid

Saleh M. Shalem[1*], Mohammed O. Daw[2], Agila S. Agila[3], Abdulwahab A. Jarbou[4], Hasan S Majdi[5]
[1,2,3]Faculty of Electrical and Electronic Engineering, University of Benghazi, Libya.
[4]Electric & Electronic Department, The Higher Institute of Science and Technology, Elmarej, Libya.
[5]Department of Chemical Engineering and Petroleum Industries, Al-Mustaqbal University College, Hillah, Babylon, Iraq.

استراتيجية تحكم فعّالة لنظام تخزين الطاقة الهجين (بطارية – مكثف فائق) ضمن شبكة تيار مستمر مصغّرة قائمة على المنظومات الكهروضوئية

صالح م. شلام[1*]، محمد ع. ضو[2]، عقيلة ص. عقيلة[3]، عبد الوهاب ا جربوع[4]، حسن ش مجدي[5]
[1،2،3]كلية الهندسة الكهربائية والإلكترونية، جامعة بنغازي، ليبيا
[4]قسم الهندسة الكهربائية والإلكترونية، المعهد العالي للعلوم والتقنية، المرج، ليبيا
[5]قسم الهندسة الكيميائية وصناعات النفط، كلية المستقبل الجامعة، الحلة، بابل، العراق.

*Corresponding author: salih.abraheem@uob.edu.ly

Received: February 20, 2026	Accepted: April 06, 2026	Published: April 16, 2026

Abstract:
The proliferation of microgrid architectures, particularly direct current (DC) microgrids, has accelerated in response to the increasing penetration of renewable energy resources integrated with advanced energy storage systems. Such configurations offer notable technical advantages, including the mitigation of harmonic distortion and improved system stability. However, the inherent intermittency and stochastic behavior of renewable generation sources, such as photovoltaic (PV) arrays and wind turbines, necessitate the incorporation of energy storage solutions to enhance system reliability, operational resilience, and overall performance. In this context, the present study develops and simulates an isolated DC microgrid framework comprising a photovoltaic generation unit, a hybrid energy storage system integrating batteries and supercapacitors, interfacing power electronic converters, and a constant load profile. A proportional–integral (PI)-based energy management strategy is implemented to regulate power flow, ensure efficient energy distribution, and sustain stable islanded operation. The control architecture further incorporates maximum power point tracking (MPPT) for optimal PV energy extraction, state-of-charge (SOC) regulation for storage coordination, and advanced converter control mechanisms to preserve DC bus voltage stability. Additionally, a relay-based protection scheme is deployed to mitigate the risk of excessive battery depth-of-discharge. The system model is developed within the MATLAB/Simulink environment, enabling comprehensive dynamic analysis under varying operating conditions. Simulation results substantiate the capability of the proposed microgrid configuration to reliably satisfy load demand while maintaining voltage regulation and operational stability. These findings validate the robustness and effectiveness of the proposed energy management strategy in addressing the challenges associated with renewable energy intermittency in islanded DC microgrid systems.

Key Words: Solar photovoltaic, MPPT, DC microgrid, PID, energy storage system, energy management system.

الملخص:

يشهد اعتماد شبكات الميكروغريد، وخاصة شبكات التيار المستمر(DC)، تسارعًا ملحوظًا مدفوعًا بالتوسع المتزايد في دمج مصادر الطاقة المتجددة مع أنظمة تخزين الطاقة المتقدمة. وتوفر هذه البُنى مزايا تقنية بارزة، من بينها تقليل التشوهات التوافقية (الهارمونيكس) وتعزيز استقرار النظام. ومع ذلك، فإن الطبيعة المتقطعة والعشوائية لمصادر التوليد المتجددة، مثل المصفوفات الكهروضوئية (PV) وتوربينات الرياح، تفرض ضرورة دمج أنظمة تخزين الطاقة لتحسين موثوقية التشغيل، وتعزيز المرونة، ورفع الأداء العام للشبكة .في هذا السياق، تُقدّم هذه الدراسة تصميمًا ومحاكاةً لبنية شبكة ميكروغريد معزولة تعمل بالتيار المستمر، تتألف من وحدة توليد كهروضوئية، ونظام تخزين هجين للطاقة يجمع بين البطاريات والمكثفات الفائقة، إلى جانب محولات إلكترونيات القدرة وحمل ثابت. كما تم اعتماد استراتيجية لإدارة الطاقة قائمة على متحكم تناسبي– تكاملي (PI) بهدف تنظيم تدفق القدرة، وتحقيق توزيع طاقي فعّال، وضمان استقرار التشغيل في وضع العزلة .(islanded mode) ويتضمن هيكل التحكم كذلك تقنيات تتبع نقطة القدرة العظمى (MPPT) لتعظيم استخلاص الطاقة من المنظومة الكهروضوئية، وإدارة حالة الشحن (SOC) لتنسيق عمل وحدات التخزين، بالإضافة إلى استراتيجيات متقدمة للتحكم في المحولات للحفاظ على استقرار جهد ناقل التيار المستمر. علاوة على ذلك، تم توظيف منظومة حماية معتمدة على المرحلات للحد من مخاطر التفريغ العميق للبطاريات .تم تطوير نموذج النظام وتنفيذه باستخدام بيئة MATLAB/Simulink، مما أتاح إجراء تحليل ديناميكي شامل تحت ظروف تشغيل متغيرة. وتُظهر نتائج المحاكاة قدرة النظام المقترح على تلبية متطلبات الحمل بكفاءة، مع الحفاظ على تنظيم الجهد واستقرار التشغيل. وتؤكد هذه النتائج متانة وفعالية استراتيجية إدارة الطاقة المقترحة في مواجهة التحديات المرتبطة بتقلبات مصادر الطاقة المتجددة ضمن شبكات الميكروغريد المعزولة العاملة بالتيار المستمر.

الكلمات المفتاحية: الطاقة الشمسية الكهروضوئية، تتبع نقطة القدرة العظمى(MPPT) ، شبكة تيار مستمر مصغّرة، متحكمPI ، نظام تخزين الطاقة، نظام إدارة الطاقة.

INTRODUCTION:

In light of the rapid depletion of fossil fuel resources, the escalating impacts of global warming, and the continuous rise in worldwide energy demand, the transition toward clean and sustainable energy solutions has become imperative for modern power systems [1-3]. Among the various alternatives, renewable energy sources have emerged as a highly promising approach to meet the growing electrification needs while minimizing environmental impacts [4,5]. These sources encompass a wide range of technologies, including solar, wind, geothermal, biomass, and tidal energy, each offering unique advantages for sustainable power generation [6-10]. Notably, photovoltaic (PV) energy has attracted significant attention due to its exceptional scalability and substantial potential to address the increasing global electricity demand [11-14].

However, PV systems are highly influenced by weather conditions and geographic location, which can render a system solely reliant on solar energy potentially unreliable under variable conditions [15-17]. To enhance the reliability and stability of PV-based systems, energy storage devices such as batteries and ultracapacitors are often integrated, enabling continuous and dependable power supply even during periods of low solar irradiation [18-21]. In this context, DC microgrids (DCMGs) have emerged as an effective framework for integrating distributed generation units, energy storage systems (ESSs), and modern DC loads. Compared with conventional AC systems, DCMGs provide higher energy conversion efficiency, simpler architecture, and superior compatibility with PV arrays, batteries, and supercapacitors (SCs) [22-27]. Maintaining a stable DC bus voltage within these microgrids is critical for ensuring high power quality and reliable system operation [28-34].

Collectively, the integration of PV energy with energy storage within DC microgrids represents a promising solution for the future of sustainable and resilient power systems, capable of addressing both environmental challenges and the growing energy demand, However, due to the sensitivity of photovoltaic (PV) systems to varying environmental conditions, it is often challenging to consistently achieve maximum power utilization [35-38]. Therefore, Maximum Power Point Tracking (MPPT) techniques are considered a fundamental component in enhancing the performance of PV systems, as they enable continuous adjustment of the operating point to ensure optimal power extraction under different conditions, effectively regulating the maximum power point and improving the overall energy harvesting efficiency of PV systems [39-43], To enhance energy utilization efficiency and ensure the stability of microgrids, an Energy Management System (EMS) has been implemented to organize and coordinate the flow of energy between different sources and storage devices [44-46].

The system continuously monitors load conditions and dynamically regulates energy distribution to ensure network stability and enhance operational efficiency. It effectively adapts to fluctuations in both energy generation and load demand, thereby contributing to the overall reliability and sustainability of

system operation [47-49]. The literature presents a substantial body of work on DC microgrids, with particular emphasis on the development of advanced energy management strategies aimed at achieving optimal coordination between distributed generation sources and load requirements. Among these, intelligent control techniques such as fuzzy logic and artificial neural networks have been widely explored [50-55].

Furthermore, the incremental conductance method is implemented for MPPT, while the overall system is modeled and simulated using MATLAB/Simulink. The system performance is evaluated under dynamically varying environmental conditions, and the results demonstrate that a nearly constant voltage is maintained at the load, attributable to the effectiveness of the proposed energy management strategy. Additionally, a protection scheme for both the load and the battery is integrated into the system. This scheme is activated when the photovoltaic source fails to meet the load demand and the battery state of charge falls below a predefined threshold, thereby ensuring uninterrupted power supply while preventing deep battery discharge and consequently extending battery lifespan.

THE PROPOSED Architecture of the DC Microgrid system:

The proposed DC microgrid architecture, as illustrated in Figure 1, consists of a photovoltaic (PV) array equipped with a Maximum Power Point Tracking (MPPT) algorithm as the main power source, together with a battery storage system and a supercapacitor to enhance energy support and dynamic response. The system supplies DC loads and is regulated using a PI-based control strategy to maintain a stable DC bus voltage under different operating conditions. In the following sections, the main components of the DC microgrid will be discussed in detail.

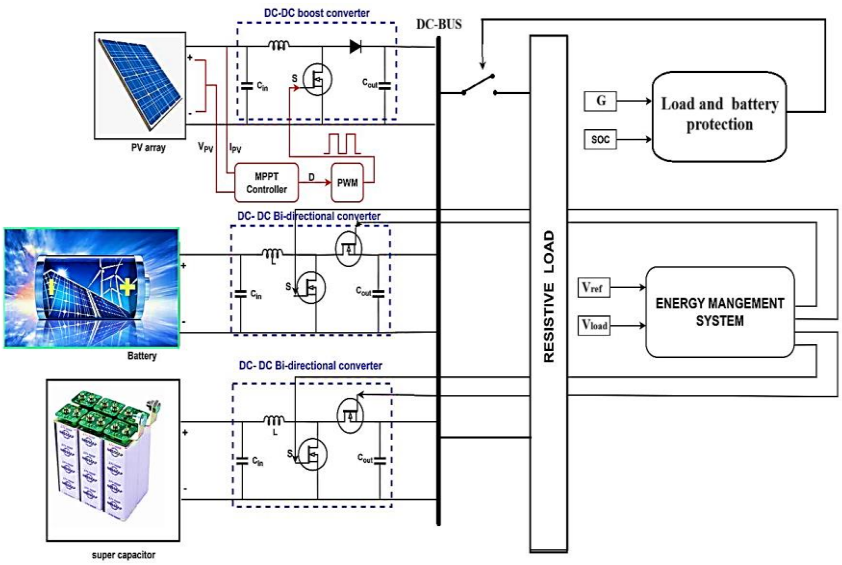

Figure (1): Proposed DC Microgrid Architecture with PV, Battery, and Supercapacitor

Modeling of PV array:

The single-diode PV cell model is illustrated by the equivalent circuit shown in Figure 2 and is commonly adopted in photovoltaic analysis due to its simplicity and adequate accuracy. The model is defined by the open-circuit voltage and the photocurrent source, which is approximately equal to the short-circuit current under standard test conditions (STC). The open-circuit voltage varies with temperature and material properties, whereas the short-circuit current is mainly influenced by solar irradiance [14].

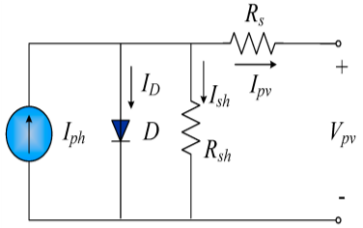

Figure (2): The single –diode model.

When a solar PV cell is subjected to solar irradiance, its output current can be determined by applying Kirchhoff's law, as shown in Equation (1).

$$I = I_{ph} - I_s - \frac{(V + IR_s)}{R_{sh}} \quad (1)$$

The photocurrent is mainly affected by the solar irradiance and the operating temperature of the PV cell, as expressed in Equation (2).

$$I_{ph} = [\, I_{SC} + K_i \,(T - T_{ref}\,)\,] \,.\, \left(\frac{G}{1000}\right) \quad (2)$$

The PV saturation current (Is) is temperature-dependent and varies as a cubic function of the PV cell temperature (T), as given in Equation (3).

$$Is = Irs\,(\frac{T}{T_{ref}})^3 \; exp\,[\frac{q.\,Eg}{K.\,A} \,.(\, \frac{1}{T_{ref}} - \frac{1}{T}\,)\,] \quad (3)$$

The reverse saturation current (Irs) can be roughly calculated using Equation 4.

$$I_{rs} = \frac{I_{sc}}{[exp\,\left(\frac{q\,V_{oc}}{N_{ser}.K\,.A\,.T}\right) - 1\,]} \quad (4)$$

IPV represents the output current of the PV system (A), while V_{PV} denotes the PV output voltage (V). T is the operating temperature of the module in Kelvin, and Tr is the reference temperature equal to 298 K. I_p refers to the photocurrent generated by solar irradiance, whereas I_o is the PV saturation current (A). A and B represent the diode ideality factor, typically taken as 1.5, and K is Boltzmann's constant ($1.38065003 \times 10^{-23}$ J/K). The symbol q denotes the electron charge ($1.60217646 \times 10^{-19}$ C), and R_s is the series resistance of the PV module. Isc is the short-circuit current under standard conditions (1000 W/m² and 25°C), while K_i is the temperature coefficient of the short-circuit current (0.102 mA/°C). λ represents the solar irradiance level (1000 W/m²), and Ego is the silicon band gap energy (1.1 eV). Finally, Np and Ns denote the number of cells connected in parallel and series, respectively.

The power output of a PV cell is described by its I–V and P–V characteristics under different temperature and irradiance conditions. The results in Figures 3 and 4 for the PV model used in this study show that voltage decreases with increasing temperature, while current increases with higher solar irradiance. The P–V curve identifies the maximum power point (MPP), which varies with environmental conditions.

The principal parameters of the photovoltaic (PV) module used in this study are provided in Table I. These parameters, including short-circuit current, open-circuit voltage, maximum power, and temperature coefficients, are essential for accurately representing and modeling the PV cell behavior.

Table (I): electrical parameters for the PV panel.

Quantity	Value	Unit
Vmpp	53.7	V
Impp	3.92	A
Pmpp	210	W
Voc	65.7	V
Isc	0.71	A
Ki	0.102	mA/℃
Kv	-0.36099	mV/℃

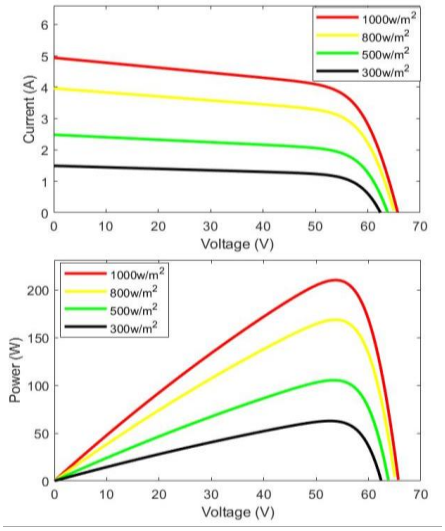

Figure (3): Current–Voltage (I–V) and Power–Voltage (P–V) Characteristics of a PV Module under Different Solar Irradiance Levels

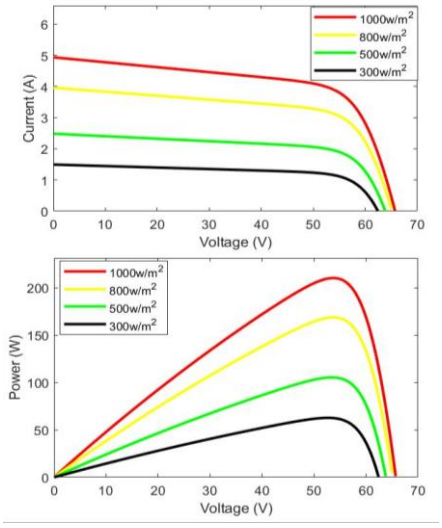

Figure (4): Current–Voltage (I–V) and Power–Voltage (P–V) Characteristics of a PV Module under Different Temperature Levels

DC-DC CONVERTER:

DC–DC converters are essential components in power engineering, used to regulate voltage levels according to system requirements. Among the main types, the Boost converter increases the voltage, while the Bidirectional converter allows power flow in both directions, making it suitable for energy storage systems such as batteries. In general, DC–DC converters are classified as step-up, step-down, and bidirectional based on their function in the system.

A. Analysis of a DC-DC boost converter:

A A DC–DC boost converter is used to step up a DC input voltage to a higher level and is widely applied in renewable energy and photovoltaic systems. The operation of this converter can be divided into two main states. In the first state, when the MOSFET is turned ON, current flows through the inductor (L), allowing it to store energy in the form of a magnetic field, while the output capacitor (C2) supplies energy to the load or inverter. In the second state, when the switch is turned OFF, the stored energy in the inductor combines with the input source, resulting in a higher output voltage. A basic boost converter circuit, as illustrated in Figure 5. demonstrates this operating principle.

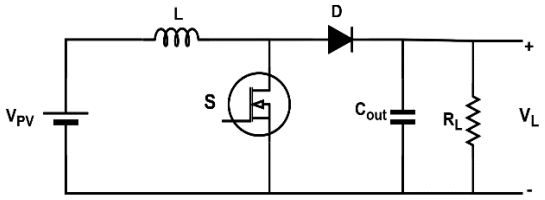

Figure (5): Schematic Diagram of a DC–DC Boost Converter

The output voltage is greater than the input voltage, as expressed in Equation (5).

$$Vo = Vin\frac{1}{1-D} \quad (5)$$

The inductor value and the output capacitor value can also be calculated using Equations (6) and (7).

$$L = \frac{Vin\ D}{\Delta_{iL}\ f_s} \quad (6)$$

$$C_{out} = \frac{D}{R\frac{\Delta v_o}{v_0}\ f_s} \quad (7)$$

V_o represents the output voltage, V_{in} represents the input voltage, D is the duty cycle, L is the inductance value, Cout is the output capacitor value, fs is the switching frequency, ΔiL is the inductor current ripple, Δvo is the output voltage ripple, and R is the load resistance. Based on these parameters, Table II presents the calculated values used in this paper.

Table (2): Component Value of DC-DC boost Converter

Parameter	Symbols	Values
Input capacitor (uf)	C_{in}	44.126
Output capacitor (uf)	C_{out}	44.126
Inductor (mH)	L	81.4
Switching frequency (KHz)	f_s	10
Resistive load (Ω)	R	25

Analysis of a DC-DC bidirectional converter:

A bidirectional DC–DC converter is a vital component for interfacing energy storage systems, such as batteries, with microgrids, as it enables controlled power flow in both directions according to operating conditions. When excess power is available from the utility grid or distributed energy resources, the converter operates in charging mode, transferring energy from the DC bus to the battery. In contrast, during power shortages, it switches to discharging mode, allowing the battery to supply energy to the DC bus and meet load demands. In addition to managing bidirectional power flow, the converter regulates the DC-link voltage, ensuring stable and reliable system operation. Figure 6. illustrates the electrical configuration of the bidirectional DC–DC converter.

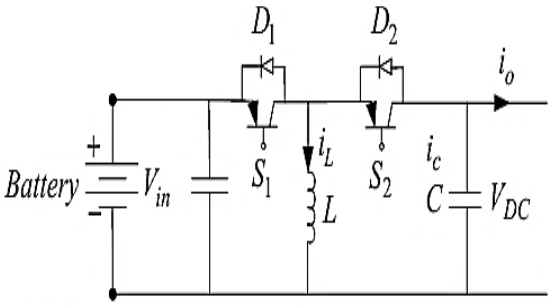

Figure (6): Schematic Diagram of a Bidirectional DC–DC Converter

The output voltage is calculated using Equation (8), whereas the values of the inductor and output capacitor are determined from Equations (9) and (10), respectively. These calculations are carried out for both modes of operation, boost and buck, depending on the converter's operating condition.

$$Vout = \begin{cases} Vin.D, \text{In buck mode} \\ \dfrac{Vin}{1-D}, \text{ In boost mode} \end{cases} \quad (8)$$

$$L = \begin{cases} \dfrac{D(Vin - Vout)}{\Delta I_L \, f_s} & \text{In buck mode} \\ \dfrac{Vin\, D}{\Delta I_L \, f_s} & \text{In boost mode} \end{cases} \quad (9)$$

$$Cout = \begin{cases} \dfrac{\Delta I_L}{8 f_s \Delta Vout} & \text{In buck mode} \\ \dfrac{D\, I_{out}}{\Delta Vout\, f_s} & \text{In boost mode} \end{cases} \quad (10)$$

Table 3 presents the calculated values obtained in this paper.

Table (3): Component Values of Bidirectional DC–DC Converter

Parameter	**Symbols**	**Values**
Input capacitor (uf)	C_{in}	57.87
Output capacitor (uf)	C_{out}	57.87
Inductor (mH)	L	85.3
Switching frequency (KHz)	f_s	10

MPPT Algorithm:

MPPT techniques are used to regulate the power generated from a PV array in order to extract the maximum available energy under varying solar irradiance conditions, thereby improving system efficiency. The Incremental Conductance method is considered one of the simplest and most widely used techniques. In this paper, the Incremental Conductance technique is adopted, and its modeling and simulation are presented for a PV system.

The Incremental Conductance (INC) method is based on the principle that the slope of the PV array power curve is zero at the Maximum Power Point (MPP), positive to the left of the MPP, and negative to the right, as illustrated in Figure 7. This relationship is mathematically expressed in Equation (11)

$$\begin{cases} {}^{dP}/_{dV} = 0 & at\ MPP \\ {}^{dP}/_{dV} > 0 & Left\ of\ MPP \\ {}^{dP}/_{dV} < & Right\ of\ MPP \end{cases} \quad (11)$$

The Maximum Power Point (MPP) is tracked by comparing the instantaneous conductance (I/V) with the incremental conductance (ΔI/ΔV), as illustrated in the flowchart in Figure 8. and expressed in Equations (12)– (13). The reference voltage (V_{ref}) defines the operating point of the PV array. At the MPP, V_{ref} becomes equal to VMPP, and the system continues to operate at this point unless a change in Δ_I is detected, indicating variations in environmental conditions and a shift in the MPP. In such cases, the algorithm adjusts V_{ref}, either increasing or decreasing it, to track the new MPP.

$$\frac{dP}{dV} = \frac{d(IV)}{dV} = I + V\frac{dI}{dV} \cong I + V\frac{dI}{dV} \quad (12)$$

Eq. (11) can be rewritten as:

$$\begin{cases} \frac{\Delta I}{\Delta V} = -\frac{I}{V} & at\ MPP \\ \frac{\Delta I}{\Delta V} > -\frac{I}{V} & Left\ of\ MPP \\ \frac{\Delta I}{\Delta V} < -\frac{I}{V} & Right\ of\ MPP \end{cases} \quad (13)$$

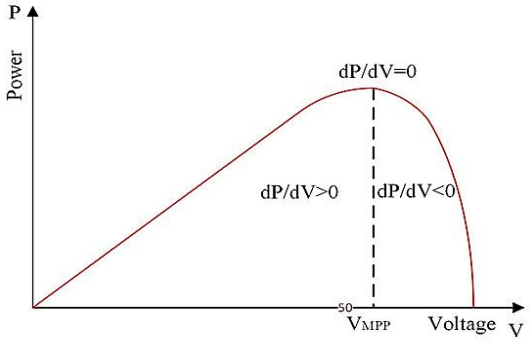

Figure (7): Principle of Incremental Conductance (INC) MPPT Method

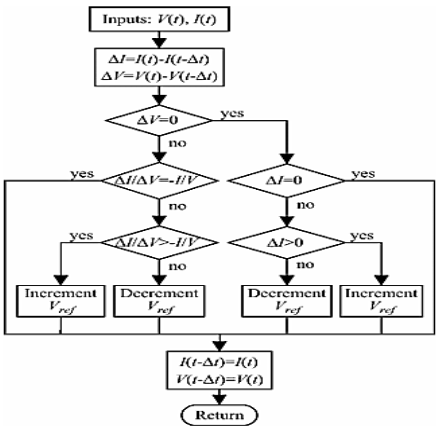

Figure (8): Flowchart of Incremental Conductance (INC) MPPT Algorithm

ENERGY STORGE SYSTEM (ESS):

Energy storage systems are utilized to support the performance of the DC microgrid when the primary source is insufficient to meet the load demand. When the photovoltaic system cannot supply the required power, both a battery and a supercapacitor are employed to ensure continuous and stable operation. These components will be discussed in detail in the following sections.

BATTERY:

The integration of batteries and supercapacitors within renewable energy systems and DC microgrids is essential for effective energy management, as it enables the storage of excess generated energy and its utilization during periods of power shortage. In this paper, a lithium-ion battery is employed, and its specifications and parameters are presented in Table IV. Battery behavior can be represented using three main types of models: mathematical models, electrochemical models, and equivalent circuit models. Among these, the equivalent circuit model is the most widely used in practical applications due to its simplicity and its ability to accurately represent battery dynamics without excessive complexity. The equivalent circuit model represents the battery as an open-circuit voltage source combined with electrical elements that reflect its internal characteristics. As illustrated in Figure. 9, the model includes the battery voltage V_b, the battery current I_b, and the open-circuit voltage V_{oc}, which is a function of the state of charge (SOC). It also incorporates polarization elements represented by resistance R_p and capacitance C_p, in addition to the internal resistance R_s, which accounts for internal losses within the battery.

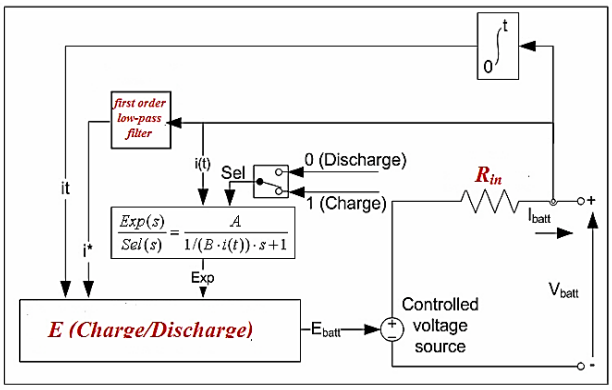

Figure (9): Battery equivalent circuit

In the discharging mode, the battery voltage can be expressed by Equation (14):

$$V_{batt} = E_O - k\left(\frac{Q}{Q - It}\right)i^* - k\left(\frac{Q}{Q - It}\right)it + Ae^{-Bit}\ (i^* > 0) \quad (14)$$

In the charging mode, the battery voltage is described by Equation (15).

$$V_{batt} = E_O - k\left(\frac{Q}{It + 0.1Q}\right)i^* - k\left(\frac{Q}{Q - It}\right)it + Ae^{-Bit}\ (i^* < 0) \quad (15)$$

The voltage at the fully charged state is given by Equation (16).

$$Vfull = E_O - Ri + A \quad (16)$$

The state of charge (SOC) is estimated using the Coulomb counting method by integrating the battery current over time during charging and discharging, as expressed in the following equation:

$$Soc = SOCo - \frac{1}{Qn}\int_0^4 \eta i\, dt \quad (17)$$

The battery model parameters are defined as follows: E_o represents the constant voltage, K denotes the polarization constant, i* is the low-frequency current component, it corresponds to the extracted capacity, A is the exponential voltage V, and B is the exponential capacity. In addition, SOC_0 denotes the initial state of charge, and Q represents the maximum battery capacity.

Table (4): Electrical Parameters of the Battery

Battery parameters		
No.	**Quantity**	**Values**
1.	Nominal voltage (V)	65
2.	Rated capacity (Ah)	4
3.	Initial state of charge (%)	90
Battery discharge parameters		

No.	Quantity	Values
	Maximum capacity (Ah)	0.05
	Fully charged voltage (V)	70
	Nominal discharge current (A)	2.80
	Capacity (Ah) at nominal voltage	0.048

SUPERCAPCITORS:

The supercapacitor (SC) is combined with the battery to mitigate peak current stress under highly dynamic load conditions by leveraging its high-power density, while the battery is responsible for supplying the average power demand. Thanks to its rapid response, high efficiency, and long cycle life, the SC effectively handles transient power fluctuations.

The key parameters of the supercapacitor, including its self-discharge characteristics, are summarized in Table (V). Figure 10 presents the electrical equivalent circuit of the SC, where (C) denotes the capacitance, (EPR) represents the equivalent parallel resistance, and (ESR) corresponds to the equivalent series internal resistance.

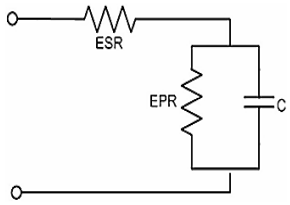

Figure (10): Electrical equivalent circuit for the SC

The energy extracted from the supercapacitor, E_{UC} can be calculated using Equation (18).

$$Euc = \frac{1}{2}C(V_i^2 - V_f^2)Euc \quad (18)$$

where the term $(V_i^2 - V_f^2)$denotes the variation between the initial and final voltage levels. The arrangement of capacitors within the supercapacitor (SC), whether in series or parallel, is selected according to the desired terminal voltage. Consequently, the overall capacitance and resistance of the SC can be determined as follows:

$$R_{total} = n_s \frac{ESR}{n_p} \quad (19)$$

$$ESR = \frac{\Delta V_d}{I_d} \quad (20)$$

$$C_{total} = n_p \frac{C}{n_s} \quad (21)$$

$$C = I_d \frac{t_2 - t_1}{V_2 - V_1} \quad (22)$$

Table (5): Electrical Parameters of the Supercapacitor (SC)

Supercapacitor (SC) main parameters		
No.	**Quantity**	**Values**
1.	Rated capacitance(F)	58
2.	Equivalent DC series resistance (Ohms)	8.9×10^{-3}
3.	Rated voltage(V)	70
4.	Initial voltage(V)	70
Self-Discharge		
No.	**Quantity**	**Values**
	Current prior open-circuit(A)	10
	Voltage at 0 s, 10 s, 100 s, and 1000 s [Voc, V3, V4, V5] (V)	[48, 47.8 ,47.06 44.65]
	Charge current [i_1, i_2, i_3, ...] (A)	[10, 20 ,100, 500]

CONTROL DESIGN FOR THE DC MICROGRID:

This section describes the design of the control systems developed in this paper for energy management and voltage regulation.

PI controllers are among the most widely used control techniques in engineering applications, as they rely on comparing the measured DC bus voltage (V_{load}) with the reference voltage (V_{ref}) to generate the voltage error signal (e_v). The control process begins with the initialization of system parameters, followed by the calculation of the voltage error as the difference between the reference and measured

values. The obtained error is then processed through an outer PI controller (voltage loop) to generate a reference current (I_{ref}). This reference is passed through a low-pass filter (LPF) to decompose it into two components: the battery reference current (I_{ref}_bat) and the supercapacitor reference current (I_{ref}_sc). Subsequently, current errors are calculated by comparing these reference values with the actual currents (I_{ref}_bat , (I_{ref}_sc)) These errors are fed into inner PI controllers (current loops), which generate the corresponding duty cycles (D_{bat}, D_{sc}) for controlling the converters. Figure 11 illustrates the flowchart of the proposed control strategy for the DC microgrid. Under low solar irradiance conditions, when the photovoltaic system is unable to meet the load demand, both the battery and the supercapacitor are engaged to compensate for the power deficit. The battery supplies the required energy, while the supercapacitor mitigates rapid load fluctuations, thereby enhancing system stability.

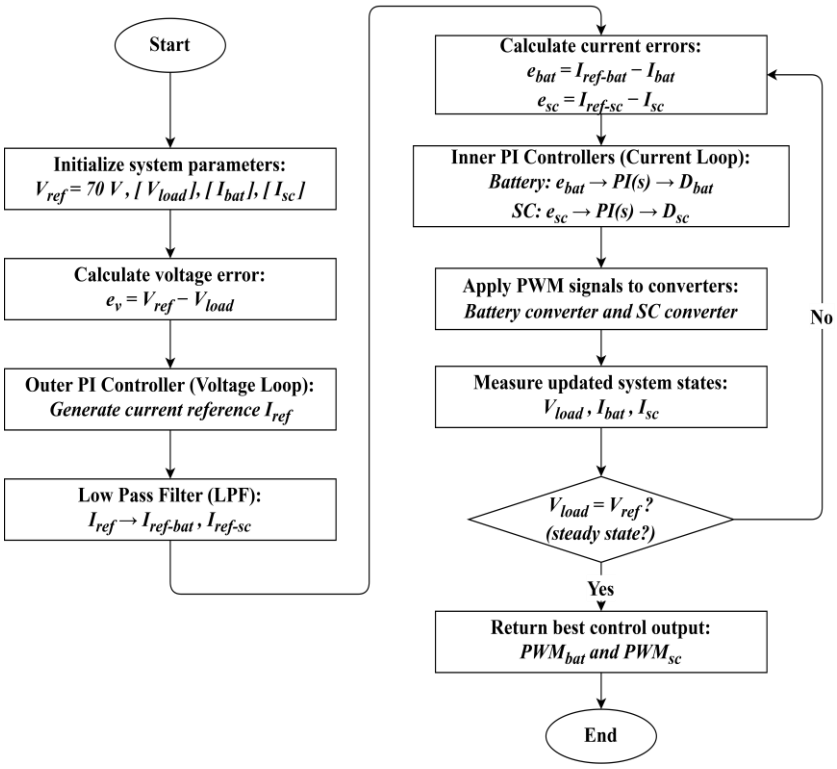

Figure (11): Control Strategy Flowchart for DC Microgrid

Conversely, in the case of surplus power, the excess energy is directed to charge both the battery and the supercapacitor through bidirectional converters. The control action is implemented via PWM signals generated by the PI controllers to regulate power flow according to system conditions. The control process continues iteratively by updating system measurements and comparing them with the reference values until the steady-state condition (V_{load} = V_{ref} = 70) is achieved, ensuring a balanced and reliable operation of the system.

The output of the PI controller can be expressed as:

$$u(s) = K_p e(s) + \frac{K_I}{s} e(s) \qquad (23)$$

Accordingly, the transfer function is given by:

$$H(s) = \frac{u(s)}{e(s)} = K_p + \frac{K_I}{s} \qquad (24)$$

$$e(s) = \left| v_{ref} - v_{DC} \right| \qquad (25)$$

The proportional gain (Kp) improves system response by reducing the rise time; however, it cannot eliminate the steady-state error, while the integral gain (Ki) removes this error with a slight effect on the dynamic performance. Here, (s) represents the Laplace operator. In this paper, the PID controller parameters (Kp, Ki) are tuned using a trial-and-error approach, by iteratively adjusting the values based on the system response until satisfactory performance in terms of stability and transient response is achieved. Additionally, an energy management function is implemented using relay-based logic to control the switching between power sources based on solar irradiance and the battery state of charge (SoC). A minimum irradiance threshold of 805 W/m² is defined to ensure sufficient power supply from the photovoltaic system; accordingly, the relay is activated (ON) at this level, indicating that the PV

array can adequately meet the load demand. Conversely, the relay is deactivated (OFF) at 800 W/m² when the generated power becomes insufficient. Similarly, battery operation is governed by predefined SoC limits. The relay is enabled when the SoC reaches 90%, indicating that the battery is capable of supplying the load in the absence of adequate solar power. It is switched OFF at 25% SoC to prevent deep discharge and extend the battery lifespan. The outputs of both relays are then processed through a logical OR gate to determine the appropriate operating mode, ensuring continuous and reliable power supply to the load. Table VI summarizes the operating conditions under different scenarios based on the relay states and the logic gate output.

Table (6): Relay-Controlled Operating Modes of the Hybrid DC Microgrid

Relay pv	Relay Soc	OR Gate Output	System operating mode
OFF	OFF	0	Both sources unavailable, system disconnects to protect components
OFF	ON	1	Battery supplies the load
ON	OFF	1	Solar panel supplies the load
ON	ON	1	system operates normally

RESULTS AND DISCUSSION:

The proposed hybrid DC microgrid system comprises a primary renewable energy source represented by photovoltaic (PV) panels, in addition to hybrid energy storage units including a battery and a supercapacitor. The PV modules employed in this paper are SunPower-based 10W Mini PV Module (EYONGPV EYE10-18SP). To meet the required power demand, the PV array is configured into seven parallel strings, each consisting of three series-connected modules, yielding a total maximum power of approximately 210.5 W. Figure 12 presents the developed simulation model implemented in MATLAB/Simulink. Considering that the performance of PV systems is highly dependent on environmental conditions particularly solar irradiance the system was evaluated under varying irradiance levels, as illustrated in Figure 13. The irradiance profile was defined as follows: 1000 W/m² from 1 s to 10 s, reduced to 800 W/m² from 10 s to 20 s, further decreased to 600 W/m² from 20 s to 30 s, then to 300 W/m² from 30 s to 40 s, and finally reaching a minimum of 100 W/m² from 40 s to 73.6 s, before returning to standard conditions (1000 W/m²). Figure 14 illustrates the PV output characteristics, including voltage, current, and power under these dynamic conditions. Meanwhile, Figure 15 depicts the battery performance in terms of voltage, current, and power. At an irradiance level of 1000 W/m², the battery operates in charging mode due to the excess power generated by the PV array. However, when the irradiance drops below 805 W/m², the PV system alone becomes insufficient to meet the load demand, thereby requiring battery support. Under these conditions, the battery supplies approximately 32 W at 800 W/m², increases its contribution to around 74 W at 600 W/m², and reaches approximately 138 W at 300 W/m². At an irradiance level of 100 W/m², the battery continues to supply the load until t = 72.66 s, at which point the state of charge (SOC) falls below 25%.

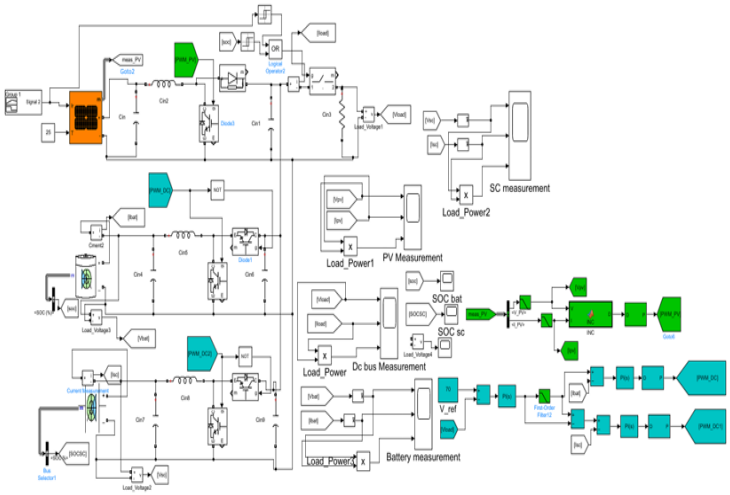

Figure (12): Hybrid DC Microgrid Simulation Model

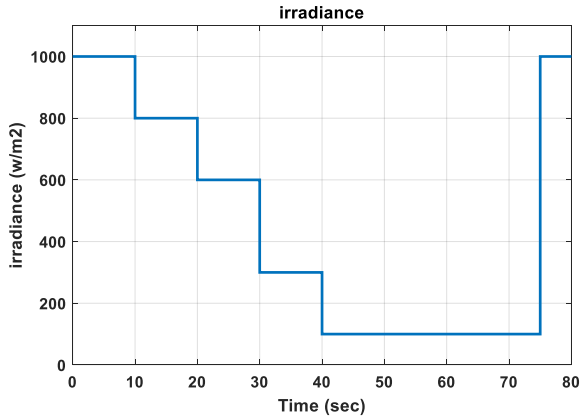

Fig (13): Solar Irradiance Profile

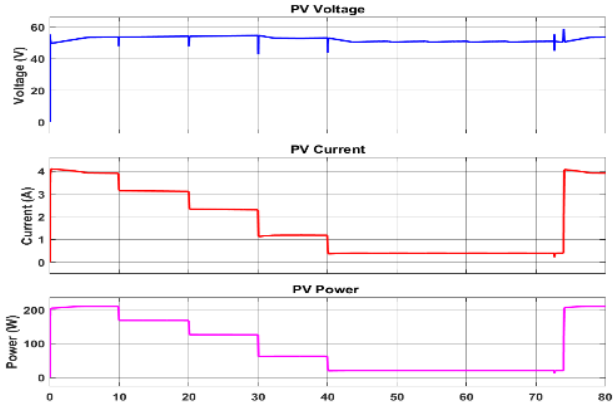

Figure (14): Performance Characteristics of PV Array under Different Irradiance Levels

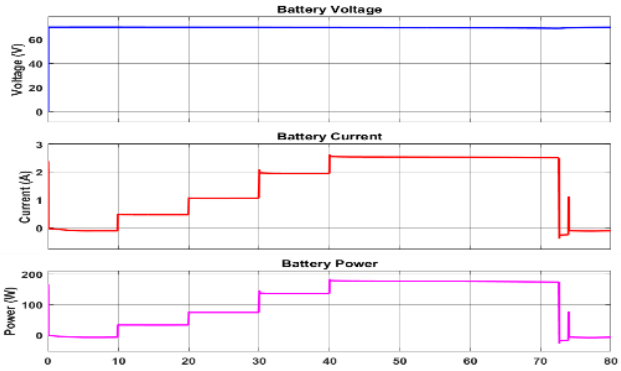

Figure (15): Dynamic Charging and Discharging Behavior of Battery in Hybrid DC Microgrid

At this stage, the relay-based protection mechanism is activated to prevent deep battery discharge, resulting in temporary load disconnection until sufficient charging is restored. Figure 16 shows the SOC profile, which decreases progressively with declining irradiance until reaching its minimum threshold at t = 72.66 s. The load remains disconnected until t = 73.66 s, after which it is reconnected once the irradiance returns to 1000 W/m², allowing the PV system to resume full load supply. Table VII summarizes the power sharing among the PV system, battery, and load across different operating intervals. Additionally, Figure 17 highlights the crucial role of the supercapacitor, which effectively compensates for rapid and transient fluctuations in irradiance by supplying instantaneous power. However, its contribution is inherently limited to short durations due to its relatively low energy storage capacity. Finally, Figure 18 demonstrates that the load power remains nearly constant at approximately 200 W despite variations in solar irradiance, owing to the coordinated operation of the PV source and hybrid storage units. In cases of severe irradiance reduction combined with low battery SOC, the load is intentionally disconnected to ensure system protection, and subsequently restored when operating conditions improve. Short interruption intervals observed in the results correspond to transient states

during which the supercapacitor mitigates rapid power fluctuations until the battery resumes its dominant role. This coordinated control strategy confirms the effectiveness of the proposed system in maintaining stability and ensuring reliable power delivery under varying environmental conditions.

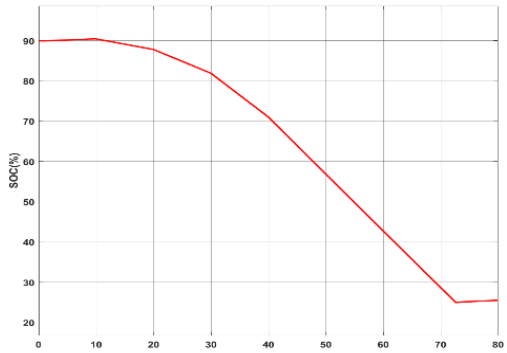

Fig (16): SOC Response of Battery Energy Storage System.

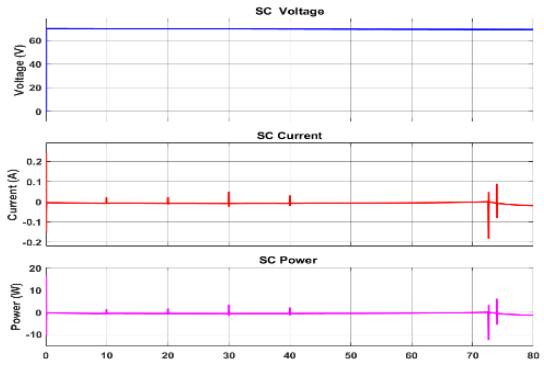

Fig (17): Supercapacitor Dynamic Response.

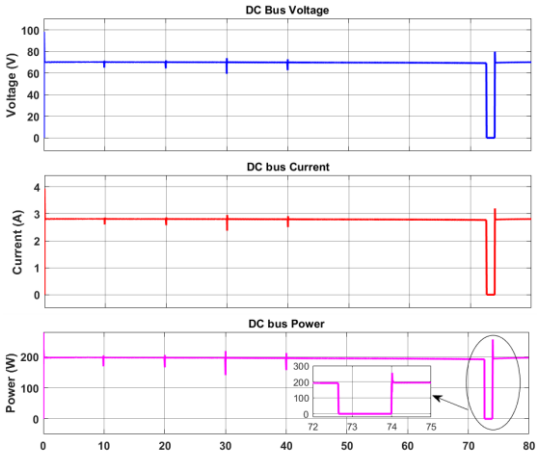

Fig (18): Load Behavior in Hybrid DC Microgrid

Table (7): Power Distribution Among PV System, Battery, and DC Load Under Different Operating Intervals

Time (sec)	Irradiance (W/m^2)	Photovoltaic power (W)	Battery power (W)	DC Load (W)
0-10	1000	210	Charging	200
10-20	800	168	32	200
20-30	600	126	74	200
30-40	300	62	138	200
40-72.66	100	20	180	200
72.66-73.66	100	20	charging	Load-protection
73.66-80	1000	210	charging	200

Conclusion:

The proposed system demonstrates high performance in hybrid DC microgrid energy management, where the Energy Management System (EMS) effectively balances power between the PV source and the hybrid storage units (battery and supercapacitor), while maintaining a stable DC bus voltage at its reference value. The MPPT algorithm achieves a high efficiency of 99.92% in extracting the maximum available power from the PV array. The battery is operated within a defined state-of-charge (SOC) range of 25%–90% to extend its lifetime and reduce stress caused by deep charging and discharging. A protection strategy is implemented that disconnects the load when the SOC drops below 25%, and reconnects it once a safe charging level is restored, ensuring safe and reliable operation of the system. Meanwhile, the supercapacitor provides fast dynamic support by compensating for rapid power fluctuations, which significantly enhances system stability under variable irradiance conditions. Future work will focus on extending the system to support AC loads through inverter integration, investigating grid-connected operation, and developing advanced energy management optimization algorithms to further improve efficiency and flexibility.

References:

[1] T. M. Aljohani, Y. O. Assolami, O. Alrumayh, M. A. Mohamed, and A. Almutairi, “Sustainable energy systems in a post-pandemic world: A taxonomy-based analysis of global energy-related markets responses and strategies following COVID-19,” *Sustainability*, vol. 17, no. 5, p. 2307, 2025.

[2] A. Barragán-Ocaña, E. Cecilio-Ayala, P. Silva-Borjas, J. A. Cortés-Ruiz, and E.-Y. Hernandez-Cardona, “Policies and sustainable energy transition in the global environment: Challenges for Latin America,” *Heliyon*, vol. 11, no. 6, p. Not Available, 2025.

[3] F. V. Bekun, M. P. Fumey, M. W. Staniewski, L. Sun, and P. O. Agboola, “Energy intensive growth and the transition pathways: Insights into the role of renewable energy and open market conditions in developing countries,” *Energy (Oxf.)*, vol. 322, no. 135192, p. 135192, 2025.

[4] M. Khaleel, Z. Yusupov, and S. Rekik, “Advancing hydrogen as a key driver for decarbonized power systems,” *Unconventional Resources*, vol. 9, no. 100278, p. 100278, 2026.

[5] B. Ahmed, Y. Nassar, H. El-Khozondar, and M. Khaleel, “Optimal design of hybrid renewable energy system (PV/wind/PHS) under multiple constraints of connection to the electricity grid: A case study,” *waujpas*, pp. 83–93, 2026.

[6] M. Khaleel *et al.*, “Evolution of emissions: The role of clean energy in sustainable development,” *Chall. Sustain.*, vol. 12, no. 2, pp. 122–135, 2024.

[7] M. Khaleel *et al.*, “Emerging issues and challenges in integrating of solar and wind,” *ijees*, vol. 2, no. 4, pp. 1–11, 2024.

[8] O. S. M. Jomah, N. Mohamed, A. A. Ahmed, A. Alsharif, M. M. Khaleel, and Y. F. Nassar, “Simulating photovoltaic emulator systems for renewable energy analysis,” in *2024 IEEE 4th International Maghreb Meeting of the Conference on Sciences and Techniques of Automatic Control and Computer Engineering (MI-STA)*, 2024, pp. 296–299.

[9] Y. F. Nassar *et al.*, “Design of reliable standalone utility-scale pumped hydroelectric storage powered by PV/Wind hybrid renewable system,” *Energy Convers. Manag.*, vol. 322, no. 119173, p. 119173, 2024.

[10] Y. F. Nassar, H. J. El-khozondar, A. A. Ahmed, A. Alsharif, M. M. Khaleel, and R. J. El-Khozondar, “A new design for a built-in hybrid energy system, parabolic dish solar concentrator and bioenergy (PDSC/BG): A case study – Libya,” *J. Clean. Prod.*, vol. 441, no. 140944, p. 140944, 2024.

[11] A. Abodwair, M. Guneser, M. Khaleel, Y. Nassar, H. El-Khozondar, and A. Elbaz, “Feasibility assessment of hybrid renewable energy based EV charging station in Libya,” *jsesd*, vol. 13, no. 2, pp. 311–349, 2024.

[12] M. Balcilar, O. Özkan, O. Usman, S. S. Akadırı, and M. A. Zambrano-Monserrate, “A global shift: How modern technologies are powering the energy transition in the face of climate change,” *J. Environ. Manage.*, vol. 384, no. 125610, p. 125610, 2025.

[13] A. Alsharif, C. W. Tan, R. Ayop, A. Ali Ahmed, M. Mohamed Khaleel, and A. K. Abobaker, “Power management and sizing optimization for hybrid grid-dependent system considering photovoltaic wind battery electric vehicle,” in *2022 IEEE 2nd International Maghreb Meeting of the Conference on Sciences and Techniques of Automatic Control and Computer Engineering (MI-STA)*, 2022.

[14] A. S. Alajmi and Z. A. Gebrel, “Thermal performance evaluation of PV technologies in hot climate environments: A review,” *ijees*, vol. 4, no. 1, pp. 01–14, 2026.

[15] T. A. Mohamed, A. A. Buaod, H. Y. Mustafa, and S. M. Saad, “Evaluating the influence of EV charging patterns on power quality metrics in modern electrical grid,” *ijees*, vol. 3, no. 2, pp. 31–46, 2025.

[16] M. Khaleel, Z. Yusupov, Y. Nassar, H. J. El-khozondar, A. Ahmed, and A. Alsharif, “Technical challenges and optimization of superconducting magnetic energy storage in electrical power systems,” *e-Prime - Advances in Electrical Engineering, Electronics and Energy*, vol. 5, no. 100223, p. 100223, 2023.

[17] A. Abudabbous, “Performance simulation of a 100 MW utility-scale solar PV plant in Sirte using Sunny Design Web,” *ijees*, vol. 3, no. 3, pp. 19–30, 2025.

[18] Y. F. Nassar *et al.*, “Regression model for optimum solar collectors’ tilt angles in Libya,” in *2023 8th International Engineering Conference on Renewable Energy & Sustainability (ieCRES)*, 2023.

[19] O. S. Abualoyoun and A. A. Amar, “Advancing the global integration of solar and wind power: Current status and challenges,” *ijees*, vol. 3, no. 2, pp. 73–88, 2025.

[20] A. Alsharif *et al.*, “Applications of solar energy technologies in north Africa: Current practices and future prospects,” *ijees*, vol. 1, no. 3, pp. 164–173, 2023.

[21] M. Almansuri, Z. Yusupov, and M. Khaleel, “Emerging trends in solar PV performance enhancement: Cooling, concentration, spectral splitting, and tracking techniques,” *ijees*, vol. 4, no. 1, pp. 32–47, 2026.

[22] A. Aghmadi, O. Ali, and O. A. Mohammed, “Stability enhancement of DC microgrid operation involving hybrid energy storage and pulsed loads,” *IEEE Trans. Consum. Electron.*, vol. 71, no. 2, pp. 3204–3217, 2025.

[23] P. Y. Reddy and L. C. Saikia, “Optimized intelligent power quality control strategy for hybrid alternating current-direct current microgrid with electric vehicle charging,” *Comput. Electr. Eng.*, vol. 124, no. 110397, p. 110397, 2025.

[24] S. M. A. Elazim *et al.*, “Enhancing stability and power quality in electric vehicle charging stations powered by hybrid energy sources through harmonic mitigation and load management,” *Sci. Rep.*, vol. 15, no. 1, p. 28077, 2025.

[25] A. Alsharif, A. A. Ahmed, M. M. Khaleel, Y. Nassar, M. A. Sharif, and H. J. El-Khozondar, “Whale optimization algorithm for renewable energy sources integration considering solar-to-vehicle technology,” in *2023 IEEE 9th International Women in Engineering (WIE) Conference on Electrical and Computer Engineering (WIECON-ECE)*, 2023, pp. 397–401.

[26] M. Khaleel, Z. Yusupov, N. Yasser, and H. J. El-Khozondar, “Enhancing Microgrid performance through hybrid energy storage system integration: ANFIS and GA approaches,” *ijees*, vol. 1, no. 2, pp. 38–48, 2023.

[27] M. Khaleel, I. Imbayah, Y. Nassar, and H. J. El-Khozondar, “Renewable energy transition pathways and net-zero strategies,” *ijees*, vol. 3, no. 4, pp. 01–16, 2025.

[28] A. A. Ahmed, M. Mohamed, Y. Nassar, and A. Alsharif, “Recent trends in optimization objectives for power system operation improvement using FACTS,” *ijees*, vol. 3, no. 4, pp. 33–46, 2025.

[29] A. Alkhair and G. A. M. Ghalboun, “Environmental impacts on energy storage systems integrated with renewables,” *ijees*, vol. 4, no. 1, pp. 15–31, 2026.

[30] M. Khaleel, Z. Yusupov, H. J. El-Khozondar, and A. Alsharif, “Cyber-resilience strategies for smart microgrids: Classification, construction, recent trends, and policy framework,” *ijees*, vol. 3, no. 3, pp. 31–47, 2025.

[31] A. Tighirt, M. Aatabe, F. E. Guezar, H. Bouzahir, and A. N. Vargas, “Power management and control of a standalone DC microgrid with hybrid renewable energy and battery storage under stochastic load conditions,” *J. Energy Storage*, vol. 152, no. 120510, p. 120510, 2026.

[32] A. Bakeer, S. Hussain, A. Chub, H. S. Salama, and G. Magdy, “Energy storage-enabled fractional-order virtual synchronous generator for DC-link voltage regulation in DC microgrid under load and renewable disturbances,” *Sci. Rep.*, vol. 16, no. 1, p. 12355, 2026.

[33] M. N. Malik, Q. Zhao, and S. Wang, “A Finite Control Set–Model Predictive Control method for hybrid AC/DC microgrid operation with PV, wind generation, and energy storage system,” *Energies*, vol. 19, no. 3, p. 754, 2026.

[34] D. Pratticò *et al.*, “Enhancing power quality and reducing costs in hybrid AC/DC microgrids via fuzzy EMS,” *Energies*, vol. 18, no. 22, p. 5985, 2025.

[35] A. Lasheen, H. F. Sindi, H. H. Zeineldin, and M. Y. Morgan, “Online stability assessment for isolated microgrid via LASSO based neural network algorithm,” *Energy Conversion and Management: X*, vol. 25, no. 100849, p. 100849, 2025.

[36] M. Panda, M. Chankaya, S. Mohanty, and S. D. Sandeep, “State-of-charge-based energy management strategy for hybrid energy storage system in DC microgrid,” *IEEE Access*, vol. 13, pp. 77353–77364, 2025.

[37] M. Zahid, H. M. Munir, M. Adeel, F. S. Alromithy, M. R. Altimania, and I. Zaitsev, “AI-driven optimization techniques for power quality improvement in microgrids: Trends, techniques, and future directions,” *Energy Sci. Eng.*, no. ese3.70342, 2025.

[38] M. M. Khaleel, Z. Yusupov, M. T. Güneşer, A. A. Abulifa, A. A. Ahmed, and A. Alsharif, “The effect of PEMFC on power grid using advanced equilibrium optimizer and particle swarm optimisation for voltage sag mitigation,” in *2023 IEEE 3rd International Maghreb Meeting of the Conference on Sciences and Techniques of Automatic Control and Computer Engineering (MI-STA)*, 2023, pp. 755–760.

[39] S. Rekik, I. Khabbouchi, D. Lounissi, M. Khaleel, D. Richards, and L. Kolsi, “Opportunities and challenges of solar-wind-powered hydrogen in emerging economies: A spatial and techno-economic analysis,” in *2025 Global Conference on Sustainable Energy and Net-Zero Emissions (SENZE)*, 2025, pp. 1–6.

[40] A. Hesri, M. Khaleel, and M. Ali, “Energy storage systems for EVs: Technologies, challenges, and pathways toward transportation decarbonization,” *ljsdr*, pp. 1–18, 2026.

[41] M. Khaleel, Z. Yusupov, O. M. Bshina, M. M. Dali, and W. A. Shah, “Toward renewable energy deployment in North African countries: Potential resources, investments, transition scenario, opportunities, challenges, and policy,” *Unconventional Resources*, vol. 12, no. 100363, p. 100363, 2026.

[42] I. Imbayah, A. Alsharif, M. Khaleel, A. A. Ahmed, and H. J. El-Khozondare, “Studying the Possibility of Smart Farms based on solar System Using (IoT) Technology in Libya,” *SUCP*, pp. 97–102, 2024.

[43] E. Mohamed, A. Souli, A. Beladel, and M. Khaleel, “Simulation and analysis of lightning strikes in electrical systems by MATLAB/SIMULINK and ATP/EMTP,” *ITEGAM- J. Eng. Technol. Ind. Appl. (ITEGAM-JETIA)*, vol. 10, no. 47, pp. 142–150, 2024.

[44] D. C. V. K. Reddy *et al.*, “Hybrid renewable energy microgrids with battery storage optimization for island communities,” *International Academic Journal of Innovative Research*, vol. 12, no. 3, pp. 103–112, 2025.

[45] D. C. Huynh, H. M. Pham, L. D. Ho, M. W. Dunnigan, and C. Barbalata, “Cost-optimal scheduling in electric vehicle-enabled microgrids using an improved artificial bee colony algorithm,” in *2025 12th International Conference on Electrical Engineering, Computer Science and Informatics (EECSI)*, 2025, pp. 282–287.

[46] R. B. Naorem, D. C. Das, and P. Roy, “Twin delayed deep deterministic policy gradient-based load frequency control for interconnected hybrid microgrids with renewable energy integration using a tilt–integral–derivative controller,” *Artificial Intelligence for Engineering*, vol. 1, no. 2, pp. 95–116, 2025.

[47] H. T. Chi, D. N. Tien, N. Le An, D. C. Le, T. D. Nguyen, and D. M. Pham, “Enhanced load sharing for energy storage systems in DC microgrids through modified droop control,” in *Proceedings of the International Conference on Sustainable Energy Technologies*, Singapore: Springer Nature Singapore, 2024, pp. 841–849.

[48] K. Zhou, M. Wei, and Y. Huang, “A wide-range input low-ripple bidirectional DC/DC converter for energy storage system integration with DC microgrids,” *J. Energy Storage*, vol. 154, no. 121137, p. 121137, 2026.

[49] Y. Huang, G.-P. Liu, Y. Yu, and H. Guo, “Fully actuated control strategy for nonlinear DC microgrids incorporating uncertain constant power loads,” *Control Eng. Pract.*, vol. 172, no. 106879, p. 106879, 2026.

[50] D. Singh, K. Choksi, S. Singh, and F. Luo, “Battery-assisted unified power quality conditioner for power quality improvement in tidal-driven seaport microgrids,” in *2025 IEEE Electric Ship Technologies Symposium (ESTS)*, 2025, pp. 436–443.

[51] Mohamed Khaleel; Ziyodulla Yusupov; Ali Hesri; Pirimov Odil; Rashidov Jahongir; Ibrahim Imbayah “AI Applications for Power Quality Challenges in Distribution Systems: Technical Barriers and Emerging Trends,” in 2026 IEEE 5th International Maghreb Meeting of the Conference on Sciences and Techniques of Automatic Control and Computer Engineering (MI-STA), 2026.

[52] K. Sado, J. Peskar, A. Downey, J. Khan, and K. Booth, “A digital twin based forecasting framework for power flow management in DC microgrids,” *Sci. Rep.*, vol. 15, no. 1, p. 6430, 2025.

[53] M. Almamoori, M. Almaktar, M. Khaleel, F. Mohamed, and A. Elbreki, “Assessing STATCOM-enabled reactive power control in fragile power transmission systems: A case study perspective,” *Math. Model. Eng. Probl.*, vol. 11, no. 8, pp. 2019–2028, 2024.

[54] M. M. Khaleel, M. R. Adzman, and S. M. Zali, “An integrated of hydrogen fuel cell to distribution network system: Challenging and opportunity for D-STATCOM,” *Energies*, vol. 14, no. 21, p. 7073, 2021.

[55] M. Haddadi, S. A. Gorji, and S. S. Yu, “An overview of inertia emulation strategies for DC microgrids: Stability analysis and AC microgrid analogies,” *IEEE Open J. Ind. Electron. Soc.*, pp. 1–32, 2025.